Simultaneous Ni Doping at Atom Scale in Ceria and Assembling into Well-Defined Lotuslike Structure for Enhanced Catalytic Performance

Qingqing Li[† 1], Zhen Huang[† 1, 2], Yimin Chao[4], Wei Shen[1, 2, 3], Hualong Xu*[1, 2, 3] & Renchao Che*[1].

[1] Laboratory of Advanced Materials, Fudan University, Shanghai 200438, P. R. China.

[2] Department of Chemistry, Shanghai Key Laboratory of Molecular Catalysis and Innovative Materials, Fudan University, Shanghai 200433, P. R. China.

[3] Collaborative Innovation Center of Chemistry for Energy Materials, Fudan University, Shanghai 200433, P. R. China

[4] School of Chemistry, University of East Anglia, UK

Crystalline CeO_2 catalyst with an optimized ion dopant is highly in demand for the enhancement of oxygen storage capacity and the associated catalytic performance. Here, a doping strategy with low Ni atom concentration (~1.8%) at ceria lattice sites has been developed, and catalyzed oxidation of CO has been observed at 320 °C, which is 100 °C lower than that with pure CeO_2. The outstanding catalytic performance can be attributed to the formation of a single Ni atoms doped "lotus-like" ceria solid solution with lattice distortion, crystal defects, and elastic strain, resulting in improved concentration of oxygen vacancy and enhanced lattice oxygen diffusion. Sub-Ångström-resolution, Cs-corrector scanning transmission electron microscopy and electron energy loss spectroscopy have been employed to elucidate the successful realization of single Ni atoms homogeneously doped into ceria matrix. A solid relationship between microstructure and the properties of ceria-based catalyst has been established.

Oxygen vacancy plays an important role in tuning properties of many metallic oxide nanomaterials, such as electronic[1], magnetic[2], luminescent[3], and catalytic[4] properties. Enhancing the concentration of oxygen vacancy induced by lattice distortion is an effective strategy, which determines the oxygen ion conduction. Doping can directly facilitate the formation and migration of oxygen vacancy[5,6]. It has been demonstrated by numerous researches that doping impurity atoms into crystal lattice of host materials can cause significant changes to crystal structure such as electron density, covalence imbalance, and distortion, which could enhance their performances in applications[3,7,8].

Among these metal oxides, cerium dioxide (ceria, CeO_2) and ceria-based materials have been becoming a ubiquitous constitute in catalytic systems for a variety of applications, such as the auto-exhausted gases treatment, water-gas shift reaction, fuel cells, hydrogen production and oxygen sensors, because of the facile redox functionality of cerium cations and the oxygen storage capacity (OSC)[9-15]. The redox capability and OSC depend largely on the concentration of oxygen vacancy and efficiency of oxygen migration in lattice. The density and the nature of oxygen vacancies are crucial to determine the reactivity of ceria-based catalysts, whose formation of each vacancy is accompanied by the localization of electrons left behind in Ce 4f states and a reduction of $Ce^{4+} \rightarrow Ce^{3+}$, leading to an extraordinary efficiency for reversible oxygen migration from surface to lattice[12,13]. Hence, it is urgently expected to optimize the parameters related to oxygen vacancy and oxygen migration. One effective route is to introduce dopants into ceria lattice. The substitution of Ce in ceria

lattice by aliovalent or rare-earth elements can provide an enhanced diffusivity of oxygen ions through the introduction of elastic strain in lattice[16-18]. Meanwhile, crystal defects can be induced by local distortion, lattice expansion or contraction of ceria matrix, which are important for its properties[6,19]. Energy of the activated oxygen migration and vacancy formation can thus be lowered. For example, the oxygen storage capacity of $Ce_{0.5}Pr_{0.5}O_{2-\delta}$ is much higher than that of pure $CeO_{2-\delta}$ because the dopant with different radii, concentration and valence states can distort the local atomic structure to have an optimized coordination environment. Mismatch of the size between dopants and Ce cations, the bond length between each species with oxygen could effectively improve the oxygen mobility and oxygen storage capacity[6]. In $Ce_{1-x}Zr_xO_2$ solid solution, a substantially declined formation energy of oxygen vacancy, which is 0.98 eV, has been revealed after doping of 50% Zr while that of the pure CeO_2 is 3.2 eV[20]. Both experiments and density-functional theory (DFT) studies have shown the easy formation of oxygen vacancy might enable a much more reducible surface and an effective transformation between oxygenates and reactive oxygen species in the catalytic cycles[21-24].

The incorporation of 5% La^{3+} into CeO_2 lattice has led to the formation of solid solutions which make T_{50} of soot conversion is about 130 °C lower than that of physically mixed catalyst. The easily generated active oxygen from the deformed CeO_2 structure can increase the oxygen mobility on the lattice. The facilitated $Ce^{4+} \leftrightarrow Ce^{3+}$ cycle of doped ceria could converses 98% of pulsed $^{18}O_2$ to CO_2 at 400 °C while the conversion is only 37% of the pure CeO_2[25]. Introducing either transition metallic ions

to build solid solutions or foreign elements to form composite oxides can significantly improve the catalytic activities of ceria[14,26-28]. Zhang and co-workers adopted a highly thermal stable ionic liquid for synthesizing the precursors, through which a homogeneous solid solution $Mn_{0.5}Ce_{0.5}O_2$ with ultra-high manganese doping concentration was obtained in order to lower oxygen vacancy formation energy and improve the migration of oxygen vacancies from bulk to surface[5]. Monodispersed transition-metal-substituted ceria nanoparticles prepared by the pyrolysis of homologous heterobimetallic precursors is of superior catalytic activity in CO oxidation[29]. Recently, atomic-level design based on interatomic potential and architecture-tuned reactivity of ceria nanostructures has become the focus in this field. For example, the diffusion of nonmetallic Au/Pt ions into subsurface layers and the sufficient oxygen vacancies close to the surface dramatically increased the activity in the water-gas shift reaction with La-doped ceria[30].

However, it is still difficult to synthesize impurity-free atomic-level doped ceria nanocrystals by a simple method. Given that the solid solution phase of a NiO_x–CeO_2 catalyst is responsible for the low-temperature redox activity, a Ni doped ceria with only a tiny amount of Ni atoms homodispersely doped into ceria matrix may be an ideal candidate for catalytic processes. Such Ni-doped system can lead to enhanced OSC and more oxygen vacancies because of reduced oxygen formation energy[31]. Therefore, a relatively simple method of preparing ceria-based solid solution doped by single atoms would be much more preferred, while the thorough understanding of the effect of substitutes on the mobility of oxygen ions as well as the redox property of ceria remains

a challenge to address.

Here, a homogeneous nickel doped ceria material (namely Ni-CeO_2) with a unique lotus-like morphology assembled by nanoparticles (~10 nm) has been synthesized through a facile solvothermal treatment strategy using metallic formates as the precursors. The formation evolution has been illustrated by in-situ observing the growth of Ni-CeO_2 (Fig. 1j). In order to further demonstrate that the Ni dopant is actually atomically well-dispersed inside ceria lattice, the microstructure of Ni-CeO_2 solid solution has been studied by a combined analysis with Cs-corrector scanning transmission electron microscopy (STEM), electron energy loss spectroscopy (EELS) at high energy resolution (0.35 eV) and atomic spatial resolution (70 pm). Solid solution composed of Ni doped ceria with elastic strain, lattice distortion, and crystal defect has remarkably increased concentration of oxygen vacancy and strongly enhanced mobility of oxygen ions. The synthesized Ni-CeO_2 with only 1.8% dopant, as CO oxidation catalyst, has shown a great performance even at low O_2/CO ratio condition, in contrast to the catalysts prepared by traditional doping methods.

Results

Synthesis and structure of lotus-like Ni-CeO_2. Lotus-like Ni-CeO_2 has been synthesized via a one-pot solvothermal method (Fig. 1a). Cerium(III) chloride heptahydrate and Nickel chloride hexahydrate were used as the metal precursors and mixed with polyvinylpyrrolidone (PVP, MW = 30,000) and formic acid in dimethyl sulphoxide (DMSO) at a molar ratio of 9: 1: 0.0125: 21. The mixture was added with ammonium hydroxide and kept stirring for 30 min with ultrasonic assistance under

room temperature. Then it was transferred into an autoclave with Teflon lining for solvothermal treatment at 150 °C for 6 h. Initially, the intermediates including $Ce(HCOO)_3$ and $[Ce(H_2O)_n]^{3+}$ were supposed to be generated (Fig. 1a). With the hydrothermal reaction temperature increasing, assisted by Ni^{2+} ions, these intermediates gradually changed into $Ce(OH)CO_3$ or CeO_2 in the process of nucleation and growth [32,33]. At the same time, template by PVP surfactant, these nanoparticles assembled and evolved into a unique lotus-like morphology. CeO_2 lattice with the incorporated Ni^{2+} ions was obtained after calcined at 550 °C. The uniform lotus-like Ni-CeO_2 has an average size of 10 μm which assembled by an abundant of particles with 8 – 10 nm size (Fig. 1b, d). Both lotus and petal unit are homogeneously composed of Ce, O, and Ni elements (EDX mappings in Fig. 1f-i), suggesting a successful Ni doping into the CeO_2 lattice. In comparison with Ni-CeO_2, the counterpart pure ceria (CeO_2) was prepared using the same method. However, pure CeO_2 exhibits a typical nanorod morphology (Fig. 1b, c) with an average diameter of 60 nm and length of 300 nm, even though assembled by similar nanoparticles with around 15 nm size, indicating a key role played by the1.8% Ni dopant. In order to clearly observe the formation process of Ni-CeO_2, the in-situ synthesis was monitored step by step. With the reaction time prolonging from 20 to 30 and 40 mins, the wire thickness of the product becomes thicker. At 40 min, pentagram shape was formed. Finally, based on a preferential orientation growth and an Ostwald ripening, the Ni-CeO_2 with lotus-like morphology was fabricated (Fig. 1j).

Characterization of Ni-CeO_2 catalyst. The XRD patterns (Fig. 2a) suggest a well-defined *Fm3m* face-centered-cubic ceria structure (JCPDS No. 34-0394) and there

are no distinct structure changes after the doping of Ni. The absence of any Ni-containing crystal phases confirms the high dispersion of Ni species at lattice position, instead of impurity phase formation. The (111) plane diffraction of Ni-CeO_2 has shifted slightly to lower Bragg angle compared to that of CeO_2, strongly revealing an increase of the inter-planar spacing, which is indicating the successful doping of Ni ions into the ceria lattice sites.

The surface atomic concentrations and valence states of Ce, Ni and O in Ni-CeO_2 and CeO_2 have been quantitatively characterized by XPS (Fig. 2c, d). The Ni concentration is about 1.1%, in agreement with ICP examination result approximately (Supplementary Fig. xx). Generally, the Ce3d spectrum of stoichiometric CeO_2 can be deconvoluted into ten contributions labelled as u and v, which are related to the hybridization of O2p valence band with the Ce4f level and the different spin-orbit doublets assigned to $3d_{3/2}$ and $3d_{5/2}$ of cerium[15,34]. The six peaks labelled as v, v'', v''', u, u'' u''' characteristically stand for Ce^{4+} ions, while the other four peaks labelled as v_0, v', u_0, u' specifically represent Ce^{3+} ions[35] (Fig. 2c). The co-existence of these two types of cerium ions at the surface or sub-surface for Ni-CeO_2 and CeO_2 can be identified from the fingerprint peaks of Ce^{4+} at 881.9 eV (v) 916.1 eV (u''') and Ce^{3+} at 883.8 eV (v') 901.6 eV (u'), respectively[36] (Fig. 2c). Moreover, the fraction of Ce^{3+} ion in the surface region can be quantitatively calculated through the peak area ratio of Ce^{3+} and Ce^{4+} ions, which is 0.26 (Ce^{3+} / Ce^{4+}) from Ni-CeO_2 and 0.21 on pure CeO_2 (Table 1). The increased Ce^{3+} content in Ni-CeO_2 indicates that the doping of Ni atom into ceria lattice influences the chemical environment of Ce ions, leading to an easy

reducibility of Ce^{4+}. Furthermore, the presence of Ce^{3+} ions modifies the electrostatic equilibrium between Ce and O ions and thus creates oxygen vacancies and unsaturated chemical bonds, especially at the grain boundary of ceria[37,38]. Therefore, a superior oxygen mobility from the bulk to surface can be achieved in the case of a higher concentration of Ce^{3+} in Ni-CeO_2 than that of undoped CeO_2. The deconvolution of XPS spectra of O1s from Ni-CeO_2 and CeO_2 are presented in Fig. 2c, d. The primary band at binding energy region of 528.8 – 529.2 eV can be assigned to lattice oxygen. The asymmetrical shoulder peak located at 531.0 – 531.5 eV reflects the adsorbed surface oxygen species (*i.e.* –OH), while a peak at 533.3 – 533.6 eV is related to the adsorbed water on surface[38,39]. A slight shift of the primary band to the higher binding energy can be observed from Ni-CeO_2, indicating the formation of CeO_{2-x} species on the surface or sub-surface[40].

In order to clarify the effect of Ni dopant on the bulk/surface defect formation of CeO_2, Raman spectra analysis has been carried out, see Fig. 2b. A main Raman-active mode at 462 cm^{-1} together with two weak modes at 582 and 1180 cm^{-1} can be identified in Fig. 2b, which can be assigned to the first-order F_{2g} peak related to the fluorite cubic structure of CeO_2, the defect-induced D bond, and the second-order longitudinal mode (2LO), respectively[41,42]. With doping, the main peak position at 462 cm^{-1} has shifted to 454 cm^{-1} and its shape becomes sharper, indicating that the dopant Ni breaks the symmetry of the Ce-O bond but maintains the basic structure of ceria.[43,44] In addition, the peak of D bond in Ni-CeO_2 gets broader and centers at a higher position of 627 cm^{-1} compared with that of CeO_2. The relative intensity ratio of these two peaks (denoted

as A_D / A_{F2g}) can be used to indicate the degree of crystal defects in CeO_2. The value of A_D / A_{F2g} of Ni-CeO_2 (0.0465) is much higher than that of CeO_2 (0.0119), which means a significantly increase of the amount of defects, such as oxygen vacancies in Ni-CeO_2 matrix. Hence, owing to the Ni incorporation into the ceria lattice, both oxygen vacancy and Ce^{3+} ion content have been increased.(Table.1).

Microstructure analysis of catalyst. The higher Ce^{3+} fraction (Ce^{3+} / Ce^{4+}) in the stoichiometric CeO_2 could generate high density of oxygen vacancy and enhance OSC to maintain the electroneutrality via charge transfer and coordination effect. Sub-Ångström-resolution, Cs-corrector scanning transmission electron microscopy (STEM) and EELS with 0.35 eV energy resolution have been employed to characterize the coordination and dispersion configuration of Ni in ceria lattice (Fig. 3f). The cell parameter of Ni-CeO_2 becomes larger than that of CeO_2 (Fig. 3a, 3b), which is in consistent with XRD results and is an indicator of a typical substitution occupation ($Ni^{2+} \rightarrow Ce^{3+/4+}$). Prior to the doping, the arrangements of Ce^{4+}/Ce^{3+} ions are in perfect square arrays (Fig. 3c). Post the doping of 1.8 at.% of Ni into the original CeO_2 matrix, remarkable lattice distortion, point defect and cation rearrangement can be observed (Supplementary Fig. xxx, and Fig. 3d). The cation rearrangements deviate from the original lattice pattern, leading to the broken of the original F*m3m* symmetry. Meanwhile, based on the statistical HRTEM analysis for many different regions, it can be concluded that ionic vacancy or displacement, twinning, and modulated structure exist inside the CeO_2 lattice even with Ni dopant as low as 1.8 at% .

Based on EELS spectrum imaging analysis (FEI Titan G3 60-300 Cubed), single

Ni atom can be discerned by scanning the electron beam probe. The sub-angstrom-resolution HAADF images (Fig. 3f) show clearly that the individual Ni atoms randomly are occupying the original Ce sites, confirmed by EELS acquired from single atom column (Fig. 3e, f). Fig. 2e shows the typical oxygen K-edge of ceria samples with and without 1.8% Ni-dopant. On each spectrum, fine structure consisted of three evident peaks (a-c) can be clearly identified. Peak *a* corresponds to the transition from O1s states to O2p states hybridized with Ce^{4+} 4f electrons. Both peak b and c at higher energy regions can be ascribed to the transitions from O1s states to the joint vacant states composed of O2p and 5d-e_g and 5d-t_{2g} states of Ce^{3+} and Ce^{4+}, which depend on the lattice configuration of CeO_2 crystal. The Ni-CeO_2 reactivity is determined by oxygen vacancy, which can be reflected by the fine structure (edge shape and intensity) of oxygen K-edge in EELS. The oxygen K-edge is dominated by three edges and the fine structure can be interpreted in terms of the transitions from O1s states towards Ni3d-O2p joint vacant hybridized states. It is noted that edge *c* contribution becomes weaker after Ni atoms were introduced into the original CeO_2 lattice, revealing that Ni dopant "share" partial oxygen and substitute the Ce position, thus modifying the original chemical environment. Considering the detail analysis of EELS data and crystal structure, the number of Ce^{3+} fraction in Ni-CeO_2 is higher than that in CeO_2, which is in agreement with XPS (Fig. 3d and Fig. 1c).

Fig. 2f shows the EELS core-loss edges of Ce. White lines can be observed, defined as Ce $M_{4,5}$ edges. The relative intensity ratio between them sensitively reflects the valence state fluctuation. To quantitatively study the influence of Ni dopant on the

oxygen vacancy and Ce valence state, M_5/M_4 intensity ratios of both samples were calculated using the positive part of the second derivative of the two experimental spectra after subtracting the background. Both the chemical shift of $M_{4,5}$ and the integral intensity ratio of white line M_5/M_4 accurately reveals the oxidation state of Ce^{4+} and Ce^{3+} ions: (a) absorption edges shift to higher energy with increased oxidation state; (b) M_5/M_4 ratio decreases with increased oxidation state. After doping Ni, M_4/M_5 increases from 0.98 to 1.12, indicating that more Ce^{3+} ion was generated by the introduction of Ni dopant. For one single Ni dopant atom, "white-line" features are clearly visible from the $L_{2,3}$ edges (fig. 3e). According to the electron-dipole selection rule, the Ni-$L_{2,3}$ edges corresponds to the transitions from the $2p_{1/2}$ (870 eV) and $2p_{3/2}$ (855 eV) states to the empty 3d orbitals localized at the Ni dopant atom. The integral area ratio of the covered L_3 and L_2 edges reflects the d^5 electron configurations occupied at the Ni 3d orbitals. This value is computed to be approximately 4.1, indicating the Ni valence state is about +2[45]. The ion radius of Ni^{2+} is smaller than that of Ni^0 and Ni^{1+} which results in larger mismatch to ceria and the stronger distortion of the structure.

H_2-TPR of catalysts. Temperature programmed reduction with H_2 (H_2-TPR) of ceria samples were performed to investigate the reducibility as well as the mobility of lattice oxygen. Ceria prepared with chemical precipitation method (denoted as CeO_2-CP) was used as a reference sample. The reduction peaks can be grouped in two parts labelled as area *I* and *II* (Fig. 4a). The peak in area *II* with high temperature is due to the reduction of bulk ceria[46]. It remains almost unchanged for all samples which indicates that the reduction of bulk ceria undergoes the same process and consumes

almost the same lattice oxygen. On the other hand, in area *I*, the peaks can be ascribed to the reduction of adsorbed oxygen species, surface ceria and the bulk ceria as the temperature increased[46-48]. By comparing the profile of CeO_2 with that of CeO_2-CP, the peak at 500 °C can be discerned with one becoming sharper in shape higher in intensity and shift to the lower temperature from ~ 540 °C, which shows a better reducibility of CeO_2 surface. This can be contributed to the reduction of the highly active oxygen species interacted with cerium ions at the surface as well as the high surface area of CeO_2, leading to a H_2 consumption of 0.441 mmol / g_{cat} compared with that of 0.115 mmol / g_{cat} for CeO_2-CP. Moreover, the related low reduction temperature should be owed to the effect of the increased concentration of oxygen vacancies that can facilitate the activation and migration of these oxygen ions, determine the formation of oxygen vacancies and the simultaneous replenishment process[49,50]. The reduction peak of Ni-CeO_2 in area *I* can be found downward shift to about 460 °C from 540 °C, and it is worth noting that a new peak raised at about 340 °C. Incorporating metal ions into ceria to form solid solution will enable it with enhanced redox ability due to the generated oxygen vacancies and the improved mobility of lattice oxygen[23,51,52]. Consequently, the bulk oxygen ions in Ni-CeO_2 can easily transfer to the surface and be reduced at a lower temperature. The high consumption of H_2, which is 0.658 mmol / g_{cat} for peaks in area *I*, can be largely ascribed to the reduction of highly active oxygen species as well as the bulk oxygen ions migrated to the surface, considering the doping amount of Ni was only 1.8% that highly dispersed in ceria crystalline. Taking these features into account, a ceria material with high OSC and fast lattice oxygen diffusion can be achieved by this

Ni-CeO_2 solid solution.

CO oxidation by catalyst. Fig. 4b illustrates the profiles of CO conversion for the CO oxidation as a function of temperature. The CeO_2 sample exhibits a lower T_{50} (365° C) than the CeO_2-CP sample, as expected for the catalyst prepared by this method. And the Ni-CeO_2 catalyst shows a T_{50} (268°C) shifted to a temperature lower than that of CeO_2 (365°C). This fact reveals that the activity of Ni-CeO_2 is significantly improved compared with other catalysts. As suggested, the CO oxidation over ceria is activated by the surface oxygen vacancies from which active sites are generated, and CO is mainly oxidized by the lattice oxygen[53]. Therefore, the superior catalytic performance of Ni-CeO_2 and CeO_2 can be contributed to the high density of oxygen vacancies, and the activity of Ni-CeO_2 is further improved due to the doping of Ni that well dispersed as single atoms in ceria lattice as well as the elevated migration ability of oxygen ions in this Ni doped solid solution.

Discussion

In conclusion, we have successfully fabricated and characterized Ni-CeO_2 solid solution synthesized by a simple one-pot solvothermal strategy with ultrasonic assistance. Examined by the in-situ reaction observation (Fig. 2f), the addition of PVP template was found to play an important role in forming “lotus-like” morphology in the dynamics process of self-assembling, Ostwald ripening and oriented growth. Ni ions, which are essential for the formation of solid solution phase, might uniformly occupied at the interstitial site of ceria lattice or replaced the original Ce site confirmed by our careful TEM examination (Fig. 3g). A significant contraction phenomenon of the cell

dimensions was found, which was compensated by the expansion produced by oxygen vacancies in the doped system. Due to the significant size difference between Ni and Ce ions, evident lattice distortion and atomic position rearrangement could be definitely generated (Supplementary Fig. xx). Either interstitial or substitution sites could generate lattice distortion (Supplementary Fig. xx), resulting to an enhanced oxygen ion diffusion from bulk to surface and a larger amount of oxygen vacancies than CeO_2 without any dopant. To maintain a charge balance, oxygen vacancy could lead to the surplus electrons, which could hybridize with the neighbor Ce 4f empty band. The degree of localization-delocalization transition difficulty determines the redox capability.

The strong coupling effect between Ni^{2+} 3d and Ce^{3+}/Ce^{4+} 4f hopping electrons effectively promote the oxygen storage/release capability during the catalysis of CO oxidation. Moreover, from the viewpoint of thermodynamics, the energy threshold requested by the $Ce^{4+}\leftrightarrow Ce^{3+}$ reduction could be remarkably depressed. Meanwhile, the particle size became smaller after the Ni doping. Such type of mesoporous Ni-CeO_2 has a larger accessible surface area (127.5 m^2/g) than pure CeO_2 (104.4 m^2/g) and CeO_2-CP (43.4 m^2/g) (Table 1). Ni-CeO_2 showed higher catalysis activity for CO oxidation. Even the Ni dopant is only 1.8%, T_{50} of Ni-CeO_2 is about 100 °C lower than the reference catalysts:CeO_2 and CeO_2-CP (Fig. 4b). This outcome could expand research to other metal atom species to make maximum utilization of them. A robust association between microstructure and catalysis activity was established, evidenced by the amount of oxygen vacancy, rapid of oxygen migration and solid solution forming that accounted

for excellent activity of Ni-CeO_2. Our unique microstructure information was confirmed on the basis of analyzing some combined micro-characterization techniques, such as XRD, Raman, XPS, TEM, STEM, EELS and H_2-TPR. The most convinced evidence to illustrate Ni-CeO_2 solid solution was the dopant of single Ni atom that uniformly dispersed in ceria lattice, without changing the basic *Fm3m* face-centered-cubic structure by employing sub-Ångström-resolution, Cs-corrector STEM-EELS analysis. This work highlights that doping and dispersion of minor content of Ni plays an important role in optimizing Ce^{3+}/Ce^{4+} ratio of ceria and the amount of crystal defects. Thus, the density of oxygen vacancy could be well adjusted and the rapid of oxygen migration was enhanced. The results in this study for designing single atoms highly dispersed in oxide matrix to synthesize solid solution provide valuable insights for the catalysis of the single transition metal/metal atom species dispersed in oxide lattice.

Acknowledgements

This work is supported by the Ministry of Science and Technology of China (973 Project Nos. 2013CB932901), and the National Nature Foundation of China (Nos. 11274066, 51172047, 51102050, and U1330118). This work is supported by the China Postdoctoral Science Foundation (Grant No. 2015M571487). This project was sponsored by Shanghai Pujiang Program and “Shu Guang” project of Shanghai Municipal Education Commission and Shanghai Education Development Foundation (09SG01).

Experimental section

Characterization

The morphology of the samples and the energy dispersive X-ray spectroscopy (EDS) were studied by a field emission scanning electron microscope (FESEM, HITACHI, S-4800). A FEI Titan3-G2 transmission electron microscope (TEM) equipped with dual-C_s-corrector, a post-column Gatan imaging filter (GIF-966) and a monochromator was used for High-Resolution TEM, STEM-HAADF and EELS analyses. Acceleration voltage is 300 kV and point resolution can reach 0.06 nm in TEM and 0.07 nm in STEM. The energy resolution was ~0.35 eV at 300 KV, as determined by the full-width at half-maximum (FWHM) of the zero-loss peak, so that fine structure and sight chemical shift of white lines can be reflected. EELS data were recorded with a two-dimensional back-illuminated charge-coupled device camera (4000 × 2700 pixels) with a low read-out noise and a negligible dark count noise. To avoid electron channeling effects, the selected grain was tilted slightly off the zone axis by 2-4º. The convergence angle was about 0.7 mrad ($q \approx 0.04$ Å^{-1}) and the collection angle was ~3 mrad ($q \approx 0.17$ Å^{-1}). EELS data were acquired with a dispersion of 0.01 eV per channel for monitoring the fine structure change of white lines. The digital micrograph software (Gatan) was used for image recording/processing. Both high-spatial-resolution and high-energy-resolution can be realized by Titan3-G2 TEM. The intensity ratio of white lines, $I(L_3)/I(L_2)$, are characteristic of the valence state of nickel ions. The raw EELS data was deconvoluted using a Fourier ratio technique to remove multiple-scattering effect. The backgrounds were subtracted using the standard AE^{-r}

power-law model.

In order to provide further insight into the nanostructure of the lotus-like Ni-CeO_2, the powder samples were embedded in resin and cut by ultramicrotome machine to be thin sections with a thickness below 20 nm.

The powder X-ray diffraction (XRD) measurements were acquired using a Bruker D8 X-ray diffractometer with Ni-filtered Cu Kα radiation (40 kV, 40 mA) with a 2 theta range of 10 – 90^o.

The X-ray Photoelectron Spectroscopy (XPS) measurements were recorded on KRATOS Axis Ultra Dld equipped with a monochromatic X-ray source (Al Kα, $h\nu$ = 1486.6 eV). Before the spectra acquisition the samples were pelletized and outgassed for 1 h at 50 °C, and the pressure for the analysis chamber is 10^{-9} mbar.

Raman spectra were recorded at room temperature in ambient conditions on a Renishow Invia spectrometer equipped with a Leica DMLM confocal microscope and a CCD detector with a 514 nm laser excitation.

Elemental analysis was performed on a Thermo Elemental IRIS Intrepid ICP atomic emission spectrometer. Before the analysis, each sample was dissolved in a solution of hydrogen peroxide and nitric acid and heated at 80 °C for 2 h.

The temperature programmed reduction with H_2 (H_2-TPR) was performed on a Micromeritics ChemiSorb 2720 analyzer equipped with a Thermal Conductivity Detector (TCD). Helium and 5%H_2-Argon and were used for purge and reduction, respectively. The temperature was set to 900 °C with an elevating rate of 10 ^{o}C / min and a gas flow rate of 30 ml / min.

Synthesis

All chemicals were purchased from Sigma-Aldrich Co. LLC. and used as received without further purification in the synthesis process. The deionized water used for experiments was obtained through an ultra-pure water system (Millipore, 18.2 MΩ·cm at 298 K). In a typical synthesis process involving solvothermal strategy, 0.486 mmol $CeCl_3 \cdot 7H_2O$ with 0.054 mmol $NiCl_2 \cdot 6H_2O$ for Ni-CeO_2 or 0.54 mmol $CeCl_3 \cdot 7H_2O$ for CeO_2 and 1.0 g of polyvinylpyrrolidone (PVP, MV = 30000) was added in 34 ml dimethyl sulfoxide (DMSO, AR) and dissolved by ultrasonic. After a clean solution obtained, 2 ml of 1.0 M ammonia solution was added together with 0.8 ml formic acid (98 %) and the solution was kept stirring for 0.5 h before it was transferred into a Teflon-lined autoclave of 50 ml capacity for the solvothermal treatment. The autoclave was placed into an oven of 150 °C for 6 h and then cooled to the room temperature. The product was collected by centrifugation and washed with ethanol for three times, followed by drying at 70 °C for 6 h. Finally, the product was calcined at 550 °C for 4 h with a heating rate of 2 °C / min. Then pickling the obtained products in diluted HNO3 (25%wt) for 30 minutes. The reference catalyst CeO_2-CP was prepared by chemical precipitation method, in which 0.5 mmol $CeCl_3 \cdot 7H_2O$ was dissolved in water and the pH value was adjusted to 9 ~ 10 with ammonia solution. A suspension was obtained and treated the same way with Ni-CeO_2 and CeO_2.

Catalytic performance on CO oxidation

Catalytic reactions were performed in a continuous flow, fixed-bed stainless steel reactor furnished with a quartz lining. Before each test, the catalyst was put into an oven of 100 °C for at least 2 h, and then 100 mg of catalyst was used and pre-heated under 550 °C for 1 h with an air flow rate of 20 ml / min. After the reactor cooling to the room temperature, the feedstock 1% CO with 1% O_2 in Helium was sent in and the temperature was manually set to each reaction temperature point with a heating rate of 5 °C / min. The products at different temperature were analyzed by an online GC (Thermal Trace GC), which equipped with a TDX-01 packed column (80 – 100 mesh, 2 m × 3 mm) and a thermal conductivity detector (TCD, 150 °C, 80 mA). The conversion of CO was calculated using the equation below:

$$Con_{CO} = \frac{CO_{in} - CO_{out}}{CO_{in}} \times 100\%$$

References

1. Veal, B. W. *et al.* Interfacial control of oxygen vacancy doping and electrical conduction in thin film oxide heterostructures. *Nat. Commun.* **7**, 11892 (2016).
2. Brinkman, A. *et al.* Magnetic effects at the interface between non-magnetic oxides. *Nat. Mater.* **6**, 493-496 (2007).
3. Wang, L. G. *et al.* Formation of the dopant-oxygen vacancy complexes and its influence on the photoluminescence emissions in Gd-doped HfO_2. *J. Appl. Phys.* **116**, 123505 (2014).
4. Jeen, H. *et al.* Orienting Oxygen Vacancies for Fast Catalytic Reaction. *Adv. Mater.* **25**, 6459-6463 (2013).
5. Zhang, P. *et al.* Mesoporous $MnCeO_x$ solid solutions for low temperature and selective oxidation of hydrocarbons. *Nat. Commun.* **6** (2015).
6. Ahn, K. *et al.* Role of Multivalent Pr in the Formation and Migration of Oxygen Vacancy in Pr-Doped Ceria: Experimental and First-Principles Investigations. *Chem. Mater.* **24**, 4261-4267 (2012).
7. Wang, F. *et al.* Simultaneous phase and size control of upconversion nanocrystals through lanthanide doping. *Nature* **463**, 1061-1065 (2010).
8. Albuquerque, A. R. *et al.* DFT Study on Ce-Doped Anatase TiO_2: Nature of Ce^{3+} and Ti^{3+} Centers Triggered by Oxygen Vacancy Formation. *J. Phys. Chem. C* **118**, 9677-9689 (2014).
9. Sun, C., Li, H. & Chen, L. Nanostructured ceria-based materials: synthesis, properties, and applications. *Energ. Environ. Sci.* **5**, 8475-8505 (2012).
10. Jacobson, A. J. Materials for Solid Oxide Fuel Cells†. *Chem. Mater.* **22**, 660-674 (2010).
11. Epifani, M. *et al.* The Role of Surface Oxygen Vacancies in the NO_2 Sensing Properties of

SnO_2 Nanocrystals. *J. Phys. Chem. C* **112**, 19540-19546 (2008).

12. Paier, J., Penschke, C. & Sauer, J. Oxygen defects and surface chemistry of ceria: quantum chemical studies compared to experiment. *Chem. Rev.* **113**, 3949-3985 (2013).
13. Esch, F. *et al.* Electron Localization Determines Defect Formation on Ceria Substrates. *Science* **309**, 752-755 (2005).
14. Yashima, M. Invited Review: Some recent developments in the atomic-scale characterization of structural and transport properties of ceria-based catalysts and ionic conductors. *Catal. Today* **253**, 3-19 (2015).
15. Trovarelli, A. *Catalysis by Ceria and Related Materials*. Vol. 2 (Imperial College Press, 2002).
16. Rushton, M. J. D. & Chroneos, A. Impact of uniaxial strain and doping on oxygen diffusion in CeO_2. *Sci. Rep.* **4** (2014).
17. Yashima, M. & Takizawa, T. Atomic Displacement Parameters of Ceria Doped with Rare-Earth Oxide $Ce_{0.8}R_{0.2}O_{1.9}$ (R = La, Nd, Sm, Gd, Y, and Yb) and Correlation with Oxide-Ion Conductivity. *J. Phys. Chem. C* **114**, 2385-2392 (2010).
18. Li, T., Xiang, G., Zhuang, J. & Wang, X. Enhanced catalytic performance of assembled ceria necklace nanowires by Ni doping. *Chem. Commun.* **47**, 6060-6062 (2011).
19. Tang, Y. L. *et al.* Observation of a periodic array of flux-closure quadrants in strained ferroelectric $PbTiO_3$ films. *Science* **348**, 547-551 (2015).
20. Chen, H. T. & Chang, J. G. Oxygen vacancy formation and migration in $Ce_{(1-x)}Zr_{(x)}O_2$ catalyst: a DFT+U calculation. *J. Chem. Phys.* **132**, 214702 (2010).
21. Cen, W. *et al.* A theoretic insight into the catalytic activity promotion of CeO_2 surfaces by Mn doping. *Phys. Chem. Chem. Phys.* **14**, 5769-5777 (2012).

22. Nolan, M. Hybrid density functional theory description of oxygen vacancies in the CeO_2 (110) and (100) surfaces. *Chem. Phys. Lett.* **499**, 126-130 (2010).

23. Murugan, B. & Ramaswamy, A. V. Defect-site promoted surface reorganization in nanocrystalline ceria for the low-temperature activation of ethylbenzene. *J. Am. Chem. Soc.* **129**, 3062-3063 (2007).

24. Gao, R. *et al.* Morphology-Dependent Properties of MnO_x/ZrO_2–CeO_2 Nanostructures for the Selective Catalytic Reduction of NO with NH_3. *J. Phys. Chem. C.* **117**, 10502-10511 (2013).

25. Buenolopez, A., Krishna, K., Makkee, M. & Moulijn, J. Enhanced soot oxidation by lattice oxygen via La^{3+}-doped CeO_2. *J. Catal.* **230**, 237-248 (2005).

26. Ou, D. R. *et al.* Oxygen-vacancy ordering in lanthanide-doped ceria: Dopant-type dependence and structure model. *Phys. Rev. B* **77** (2008).

27. Stroppa, D. G. *et al.* Analysis of Dopant Atom Distribution and Quantification of Oxygen Vacancies on Individual Gd- Doped CeO_2 Nanocrystals. *Chem. Eur. J.* **20**, 6288-6293 (2014).

28. Sardar, K. *et al.* Nanocrystalline Cerium − Bismuth Oxides: Synthesis, Structural Characterization, and Redox Properties. *Chem. Mater.* **22**, 6191-6201 (2010).

29. Elias, J. S. *et al.* Structure, bonding, and catalytic activity of monodisperse, transition-metal-substituted CeO_2 nanoparticles. *J. Am. Chem. Soc.* **136**, 17193-17200 (2014).

30. Fu, Q., Saltsburg, H. & Flytzani-Stephanopoulos, M. Active Nonmetallic Au and Pt Species on Ceria-Based Water-Gas Shift Catalysts. *Science* **301**, 935-938 (2003).

31. Wang, X., Shen, M., Wang, J. & Fabris, S. Enhanced Oxygen Buffering by Substitutional and Interstitial Ni Point Defects in Ceria: A First-Principles DFT plus U Study. *J. Phys. Chem. C* **114**, 10221-10228 (2010).

32. Zhang, J. *et al.* Facile Preparation of M^{n+}-Doped (M = Cu, Co, Ni, Mn) Hierarchically Mesoporous CeO_2 Nanoparticles with Enhanced Catalytic Activity for CO Oxidation. *Eur. J. Inorg. Chem.* **2015**, 969-976 (2015).

33. He, L. *et al.* Solvothermal synthesis and characterization of ceria with solid and hollow spherical and multilayered morphologies. *Appl. Surf. Sci.* **322**, 147-154 (2014).

34. Guan, B., Lin, H., Zhu, L. & Huang, Z. Selective Catalytic Reduction of NO_x with NH_3 over Mn, Ce Substitution $Ti_{0.9}V_{0.1}O_{2-\delta}$ Nanocomposites Catalysts Prepared by Self-Propagating High-Temperature Synthesis Method. *J. Phys. Chem. C.* **115**, 12850-12863 (2011).

35. Larachi, F., Pierre, J., Adnot, A. & Bernis, A. Ce 3d XPS study of composite $Ce_xMn_{1-x}O_{2-y}$ wet oxidation catalysts. *Appl. Surf. Sci.* **195**, 236-250 (2002).

36. Venkataswamy, P., Rao, K. N., Jampaiah, D. & Reddy, B. M. Nanostructured manganese doped ceria solid solutions for CO oxidation at lower temperatures. *Appl. Catal., B.* **162**, 122-132 (2015).

37. Hojo, H. *et al.* Atomic structure of a CeO_2 grain boundary: the role of oxygen vacancies. *Nano Lett.* **10**, 4668-4672 (2010).

38. Mahamallik, P., Saha, S. & Pal, A. Tetracycline degradation in aquatic environment by highly porous MnO_2 nanosheet assembly. *Chem. Eng. J.* **276**, 155-165 (2015).

39. Carrasco, J. *et al.* In situ and theoretical studies for the dissociation of water on an active Ni/CeO_2 catalyst: importance of strong metal-support interactions for the cleavage of O-H bonds. *Angew. Chem. Int. Ed. Engl.* **54**, 3917-3921 (2015).

40. Wu, Q.-H., Thissen, A., Jaegermann, W. & Liu, M. Photoelectron spectroscopy study of oxygen vacancy on vanadium oxides surface. *Appl. Surf. Sci.* **236**, 473-478 (2004).

41. Pu, Z.-Y., Lu, J.-Q., Luo, M.-F. & Me, Y.-L. Study of oxygen vacancies in $Ce_{0.9}Pr_{0.1}O_{2-delta}$ solid solution by in situ x-ray diffraction and in situ Raman spectroscopy. *J. Phys. Chem. C* **111**, 18695-18702 (2007).

42. Wu, Z. *et al.* Probing defect sites on CeO_2 nanocrystals with well-defined surface planes by Raman spectroscopy and O_2 adsorption. *Langmuir*. **26**, 16595-16606 (2010).

43. Lee, Y. *et al.* Raman analysis of mode softening in nanoparticle $CeO_{(2-delta)}$ and Au-$CeO_{(2-delta)}$ during CO oxidation. *J. Am. Chem. Soc.* **133**, 12952-12955 (2011).

44. Yen, H., Seo, Y., Kaliaguine, S. & Kleitz, F. Tailored mesostructured copper/ceria catalysts with enhanced performance for preferential oxidation of CO at low temperature. *Angew. Chem. Int. Ed. Engl.* **51**, 12032-12035 (2012).

45. Waddington, W. G., Rez, P., Grant, I. P. & Humphreys, C. J. White lines in the$L_{2,3}$ electron-energy-loss and x-ray absorption spectra of 3d transition metals. *Phys. Rev. B* **34**, 1467-1473 (1986).

46. Shan, W. Reduction property and catalytic activity of $Ce_{1-X}Ni_XO_2$ mixed oxide catalysts for CH_4 oxidation. *Appl. Catal., A.* **246**, 1-9 (2003).

47. Holgado, J. P., Ternero, F., Gonzalez-delaCruz, V. M. & Caballero, A. Promotional Effect of the Base Metal on Bimetallic Au–Ni/CeO_2 Catalysts Prepared from Core–Shell Nanoparticles. *ACS. Catal.* **3**, 2169-2180 (2013).

48. Concepcion, P. *et al.* Chemoselective hydrogenation catalysts: Pt on mesostructured CeO_2 nanoparticles embedded within ultrathin layers of SiO_2 binder. *J. Am. Chem. Soc.* **126**, 5523-5532 (2004).

49. Feng, Z. A. *et al.* Fast vacancy-mediated oxygen ion incorporation across the ceria-gas

electrochemical interface. *Nat. Commun.* **5**, 4374 (2014).

50. Yashima, M. *et al.* Crystal Structure and Oxide-Ion Diffusion of Nanocrystalline, Compositionally Homogeneous Ceria–Zirconia $Ce_{0.5}Zr_{0.5}O_2$ up to 1176 K. *Cryst. Growth Des.* **13**, 829-837 (2013).
51. Widmann, D. & Behm, R. J. Activation of Molecular Oxygen and the Nature of the Active Oxygen Species for CO Oxidation on Oxide Supported Au Catalysts. *Accounts. Chem. Res.* **47**, 740-749 (2014).
52. Liu, H. *et al.* Active Oxygen Species and Mechanism for Low-Temperature CO Oxidation Reaction on a TiO_2-Supported Au Catalyst Prepared from $Au(PPh_3)(NO_3)$ and As-Precipitated Titanium Hydroxide. *Journal of Catalysis* **185**, 252-264 (1999).
53. Xu, J. *et al.* Operando Raman spectroscopy and kinetic study of low-temperature CO oxidation on an α-Mn_2O_3 nanocatalyst. *J. Catal.* **300**, 225-234 (2013).

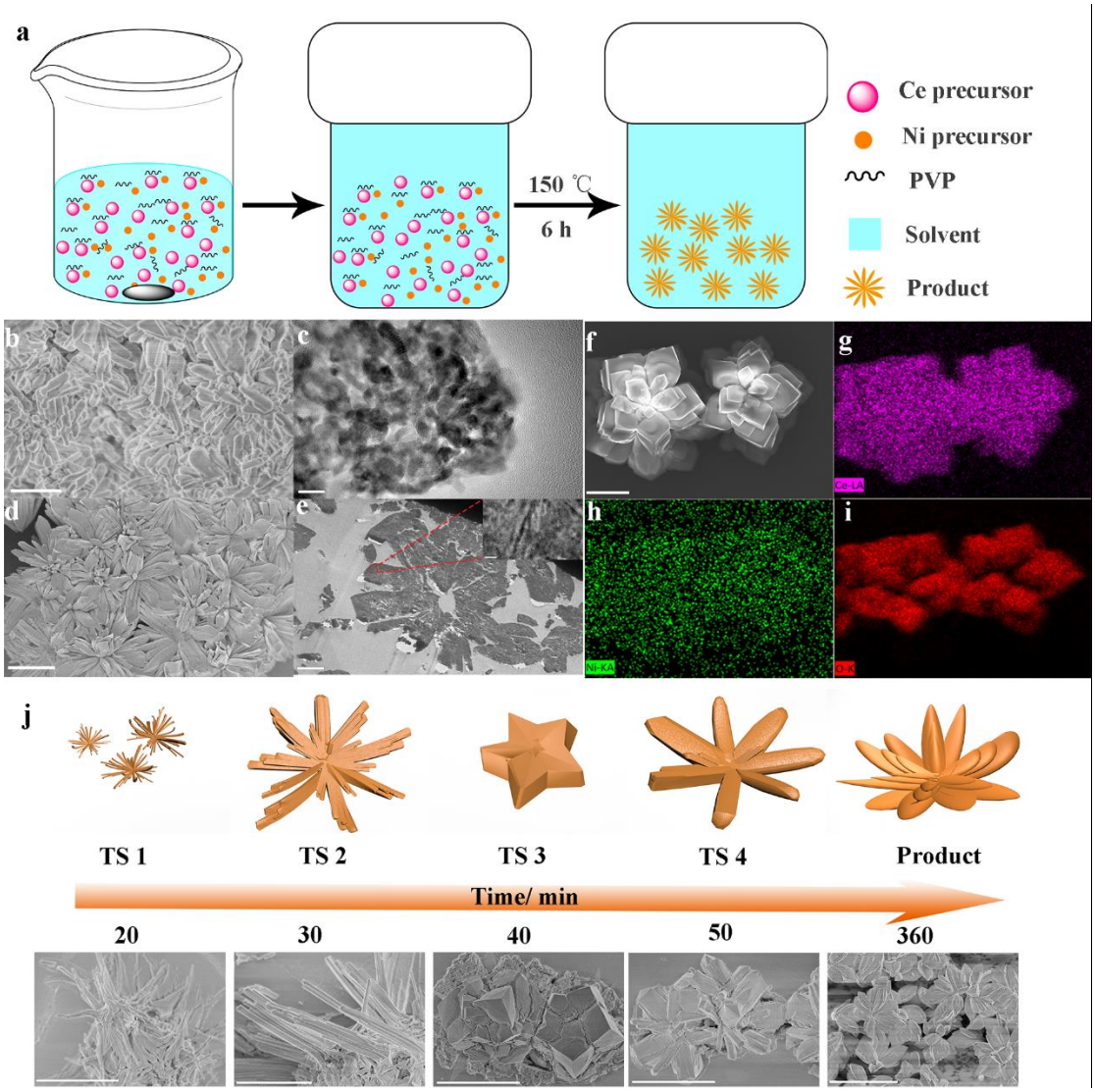

Figure 1 | Morphology and synthesis procedure of CeO_2 and Ni-CeO_2. (**a**) Schematic strategy for the preparation of lotus-like Ni-CeO_2 material *via* a one-pot solvothermal treatment. (**b**) SEM and (**c**) TEM images of CeO_2, scale bar: 500 nm and 20 nm. (**d**) SEM and (**e**) TEM images of Ni-CeO_2, the inset in (e) presents a detailed structure of selected area, scale bar: 10 μm, 2 μm, and 10 nm. (**f-i**) EDX of Ni-CeO_2, scale bar: 5 μm. (**j**) Schematic evolution of in-situ growth of lotus-like Ni-CeO_2 material, scale bar: 3 μm, 2 μm, 5 μm, 5 μm, and 10 μm, respectively.

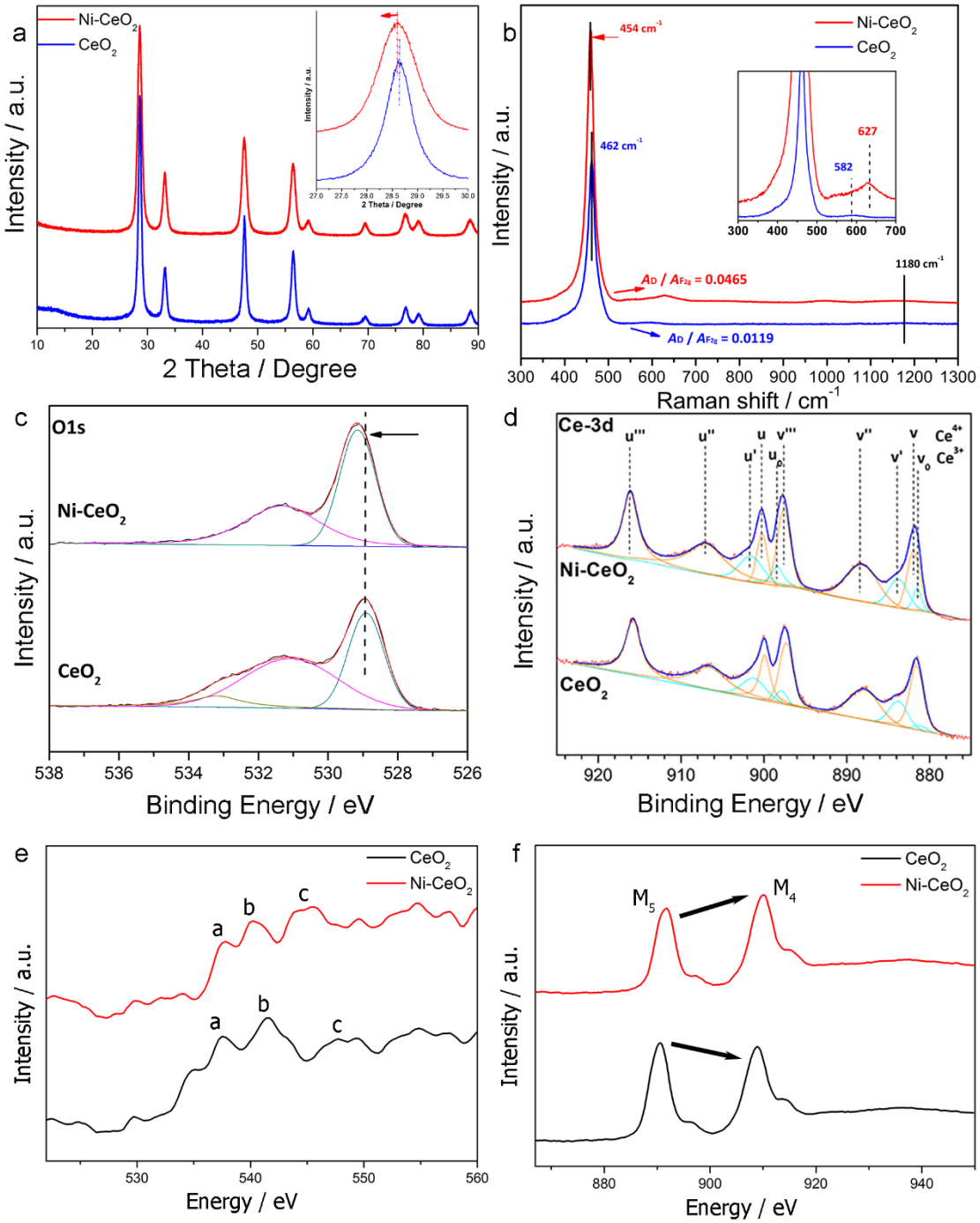

Figure 2 | Structure characterization of catalysts. (**a**) XRD pattern of CeO_2 and Ni-CeO_2. (**b**) Raman spectra of CeO_2 and Ni-CeO_2. (**c**) XPS spectra of Ce 3d and (**d**) O1s spectra of CeO_2 and Ni-CeO_2. (**e, f**) EELS results of oxygen K-edge peaks and Ce $M_{4,5}$ peaks of CeO_2 and Ni-CeO_2.

Table 1 Texture properties of CeO_2 and Ni-CeO_2.

Catalyst	Lattice Parameter *a* (nm)	Particle Size[a] (nm)	Surface Area (m^2/g)	Pore Size[b] (nm)	Dopant Content (mol%)[c]	Ce^{3+}/Ce^{4+}[d]
Ni-CeO_2	0.5407	9.3	127.5	6.74	1.8	0.26
CeO_2	0.5404	13.9	104.4	4.77	-	0.21
CeO_2-CP	0.5409	14.3	43.4	1.08	-	0.15

[a] the particle size was calculated by Scherrer equation from XRD data. [b] the pore size of catalyst was calculated by using the Barrett–Joyner–Halenda (BJH) adsorption branch of the nitrogen isotherm. [c] the content of doping metal was analysed by ICP. [d] the ratio of Ce^{3+}/Ce^{4+} was calculated from the deconvoluted Ce-3d XPS spectrum using sum of peak areas of Ce^{3+} and Ce^{4+} contributions, respectively.

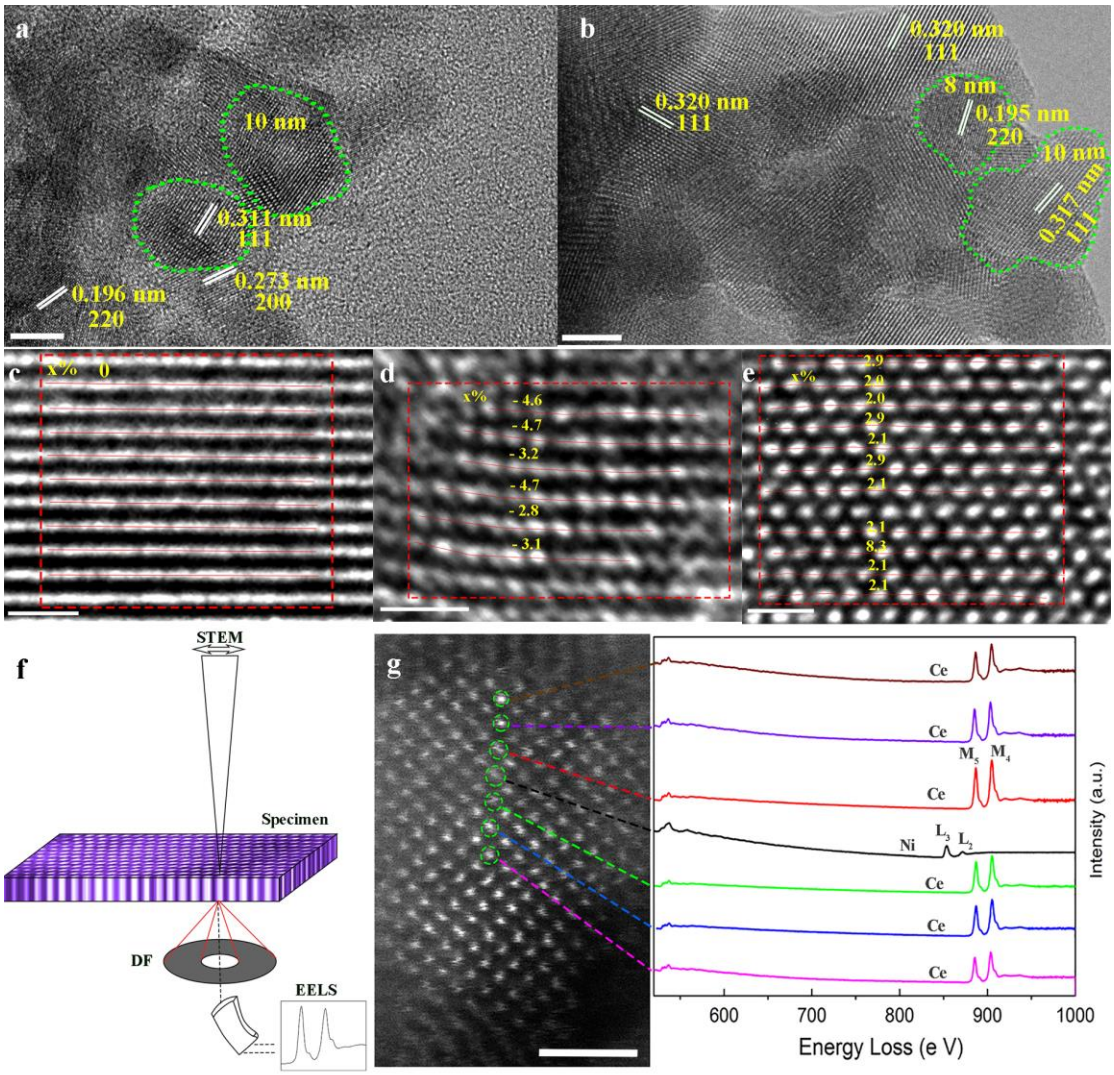

Figure 3 | Studies of the catalysts by electron microscopy. (**a, b**) HRTEM images of CeO_2 and Ni-CeO_2, scale bar: 5 nm and 5 nm. (**c**) (**d, e**) Lattice distortion of CeO_2 and Ni-CeO_2, scale bar: 1 nm, 1 nm, 1 nm. (**f**) STEM spectrum image acquisition schematic diagram. (**g**) atomic resolution HAADF-STEM image of Ni-CeO_2 (**left**), single-atom EELS results taken from the selected region (**right**), scale bar: 1 nm.

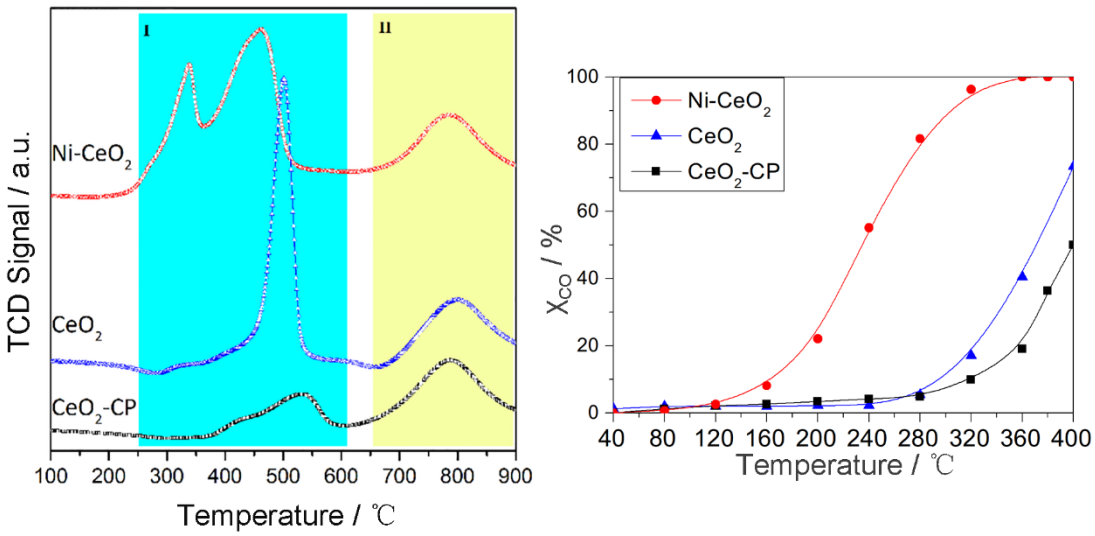

Figure 4 | Redox property of catalysts. (**a**)TPR profiles of the Ni-CeO_2, CeO_2, and CeO_2-CP samples; (**b**)Catalytic performance on CO oxidation of Ni-CeO_2, CeO_2, and CeO_2-CP. Reaction conditions: 100 mg catalyst, 1% CO and 1% O_2 with balanced He as feedstock, GHSV = 15000 h^{-1}, reaction temperature from 40 to 400 °C.